Solution Structure and Backbone Dynamics of the Human DNA Ligase IIIα BRCT Domain[†,‡]

V. V. Krishnan,[§] Kevin H. Thornton,[§,||] Michael P. Thelen, and Monique Cosman*

Biology and Biotechnology Research Program, Lawrence Livermore National Laboratory, Livermore, California 94551

Received May 14, 2001; Revised Manuscript Received August 24, 2001

ABSTRACT: BRCT (BRCA1 carboxyl terminus) domains are found in a number of DNA repair enzymes and cell cycle regulators and are believed to mediate important protein−protein interactions. The DNA ligase IIIα BRCT domain partners with the distal BRCT domain of the DNA repair protein XRCC1 (X1BRCTb) in the DNA base excision repair (BER) pathway. To elucidate the mechanisms by which these two domains can interact, we have determined the solution structure of human ligase IIIα BRCT (L3[86], residues 837−922). The structure of L3[86] consists of a $\beta2\beta1\beta3\beta4$ parallel sheet with a two-α-helix bundle packed against one face of the sheet. This fold is conserved in several proteins having a wide range of activities, including X1BRCTb [Zhang, X. D., et al. (1998) *EMBO J. 17*, 6404−6411]. L3[86] exists as a dimer in solution, but an insufficient number of NOE restraints precluded the determination of the homodimer structure. However, ^{13}C isotope-filtered and hydrogen−deuterium exchange experiments indicate that the N-terminus, α1, the α1−β2 loop, and the three residues following α2 are involved in forming the dimer interface, as similarly observed in the structure of X1BRCTb. NOE and dynamic data indicate that several residues (837−844) in the N-terminal region appear to interconvert between helix and random coil conformations. Further studies of other BRCT domains and of their complexes are needed to address how these proteins interact with one another, and to shed light on how mutations can lead to disruption of function and ultimately disease.

BRCT[1] (BRCA1 C-terminus) domains are autonomously folding units of approximately 95 residues (*1*, *2*). The name is derived from their homology with the C-terminal region of the breast cancer suppresser protein, BRCA1. Deletions and mutations within the BRCT region of BRCA1 have been identified as a high-risk factor for breast and ovarian cancers (*3*). On the basis of the experimental evidence to date, it is believed that BRCT domains recruit and bind other BRCT domains or unknown protein folds with high affinity and specificity. Thus, mutations within these domains might deleteriously affect DNA repair and other cellular pathways that rely on protein−protein interactions for normal function. Another hypothesis suggests that the BRCT domains may be molecular sensors allowing indirect or direct recognition of particular DNA structures (*4*).

Sequence analysis using hydrophobic clustering has identified the presence of 50 copies of BRCT domains in 23 different proteins involved in DNA repair, recombination, and cell cycle control (*5*). However, the three-dimensional structure of only one, the 3.2 Å X-ray crystallographic structure of the distal BRCT domain of the repair protein XRCC1 (X1BRCTb), has been determined (*6*). This structure is of an asymmetric homodimer in which each monomeric unit is comprised of a four-stranded parallel β-sheet surrounded by three α-helices (*6*). Although the XRCC1 protein has no known enzymatic function, it has been suggested that it coordinates the rapid recruitment of polymerase β, poly(ADP-ribose)polymerase (PARP), and ligase IIIα (L3α) to the DNA substrate during DNA base excision repair (BER) (*2*, *7*−*10*). While pol β interacts with the N-terminal domain of XRCC1 (*11*), PARP and L3α interact with XRCC1 via their respective BRCT domains (*2*, *8*). In addition, the coordinated expression of XRCC1 and L3α is required to maintain normal L3α activity levels in the cell (*12*, *13*).

The L3 protein is distinguished from other DNA ligases by its ability to join an oligo(rA) hybridized to a poly(dT) template (*14*) and by a unique N-terminal (residues 18−55) zinc finger motif that is homologous to a PARP DNA nick sensing zinc finger domain (*8*). Compared to other mammalian ligases, the L3 protein is also more closely related to viral ligases (*15*), which appear to play analogous roles

[†] This work was performed under the auspices of the U.S. Department of Energy by the Lawrence Livermore National Laboratory under Contract W-7405-ENG-48 and supported by Lawrence Livermore National Laboratory LDRD Director's Initiative Grants 99-LW-031 and 99-LW-068 and partly funded by NIH Grant CA76116 to M.P.T.

[‡] Coordinates for the refined average structure and the family of 20 structures have been deposited in the Protein Data Bank (entries 1IMO and 1IN1).

* To whom correspondence should be addressed. Phone: (925) 423-1647. Fax: (925) 424-3130. E-mail: cosman1@llnl.gov.

[§] These authors contributed equally to this work.

[||] Present address: Bio-Rad Laboratories Life Science Group, 2000 Alfred Nobel Dr., Hercules, CA 94547.

[1] Abbreviations: L3, human DNA ligase III; BRCT, BRCA1 C-terminus; L3[86], residues 837−922 of the BRCT domain of L3α; BER, base excision repair; XRCC1, X-ray cross complementing; X1BRCTb, second XRCC1 BRCT domain located closest to the C-terminus (residues 538−633); NOE, nuclear Overhauser effect; NOESY, NOE spectroscopy; COSY, correlation spectroscopy; TOCSY, total correlation spectroscopy; HSQC, heteronuclear single-quantum correlation; R_1, longitudinal relaxation rate; R_2, transverse relaxation rate; τ_c, rotational correlation time; SASA, solvent accessible surface area.

10.1021/bi010979g CCC: $20.00
Published on Web 10/12/2001

in the repair and recombination of the viral genome (*16*, *17*). There are two isoforms of L3, α and *β*, that have identical catalytic properties, but differ as a result of a tissue-specific alternative splicing mechanism entailing exons encoding the carboxyl terminus (*15*, *18*−*20*). The 96 kDa L3*β* is found in testes during the latter stages of meiotic prophase, whereas the 103 kDa L3α form is present at similar levels in several tissues (*21*). L3*β* does not contain the BRCT domain and is stable without XRCC1; L3α requires XRCC1 for stability (*22*). Recently, we have shown that a significant increase in thermostability is imparted by the interaction between the BRCT domains of L3α and XRCC1, which may explain why cells require XRCC1 to maintain L3α activity (*23*).

Here we report on the NMR structure and backbone dynamics of the human L3α BRCT domain (L3[86], residues 837−922) in an effort to gain further insight into the functional roles of XRCC1/L3 BRCT domains in protein−protein interactions. Our results show that the L3[86] protein adopts a core structure consisting of a *β*2*β*1*β*3*β*4 parallel sheet with a two-α-helix bundle packed against one face of the sheet. This core fold is found in several proteins having low levels of sequence homology and a broad range of functional activities.

MATERIALS AND METHODS

Sample Preparation. The expression and purification of L3[86] have been described in detail by Thornton et al. (*23*). Briefly, uniformly ^{15}N-labeled and ^{15}N- and ^{13}C-labeled L3[86] proteins (residues 837−922) were overexpressed in a BL21(DE3) *Escherichia coli* host as a glutathione *S*-transferase (GST) fusion protein in M9 minimal medium supplemented with 1 g/L $^{15}NH_4Cl$ and 5 g/L unlabeled or ^{13}C-labeled glucose, purified on a glutathione−agarose affinity column, digested with bovine thrombin, and further purified using size-exclusion chromatography. A 10% non-random fractionally ^{13}C-labeled sample was also overexpressed using minimal medium that contained 3.6 g/L unlabeled glucose and 0.4 g/L 98% ^{13}C-labeled glucose (*24*). After thrombin cleavage, the L3[86] protein has two additional non-native residues (Gly and Ser) at the N-terminus, as confirmed by mass spectrometry (SynPep, Dublin, CA). The calculated pI of L3[86] is 7.94; the calculated molecular mass is 9973 Da, and the extinction coefficient is 13 940 M^{-1} cm^{-1} at 280 nm (assuming all Cys residues are reduced) (*25*). Typical yields of labeled L3[86] were 7 mg/L of cell culture. The protein was >95% pure as determined by SDS−polyacrylamide gel electrophoresis. All NMR experiments were performed on samples dissolved in 50 mM NaH_2PO_4, 150 mM NaCl, and 25 mM d_{10}-DTT (Isotech) (pH 6.6). Final protein concentrations were 0.4−1.0 mM.

NMR Experiments. NMR experiments were carried out on a 600 MHz Varian INOVA spectrometer at 15 °C using either home-written pulse sequences or those available in the Protein Pack software package provided by Varian (Palo Alto, CA). Proton chemical shifts were referenced to the H_2O signal, while the ^{15}N and ^{13}C signals were referenced indirectly using *γ* ratios of 0.251 449 530 and 0.101 329 188, respectively. The temperature was calibrated using an external methanol sample. Spectra were processed and analyzed using Felix 97 (Accelrys, San Diego, CA). A ^{15}N-labeled sample in a 9:1 H_2O/D_2O mixture was used to acquire ^{15}N-HSQC (*26*), ^{15}N-TOCSY-HSQC (28 ms mixing time) (*27*), ^{15}N-NOESY-HSQC (50 ms mixing time) (*28*), HNHA (*29*), and SCT-HMSQC-HA (*30*) spectra. Hydrogen−deuterium (H−D) exchange kinetics were measured via a series of ^{15}N-HSQC experiments (32 scans, 40 t_1 increments, and a total acquisition time of 55 min). Buffer exchange to 100% D_2O was carried out using an Amicon 8MC Micro-Ultrafiltration System (YM10 membrane). Acquisition of the first experiment was initiated ∼150 min after the buffer exchange. A ^{13}C- and ^{15}N-labeled L3[86] sample in 95% H_2O was used to acquire the HNCO, HNCA, HN(CO)CA, CBCA(CO)NH, HNCACB, and HCCH-COSY spectra (*31*). The same sample in 100% D_2O was used to acquire the HCCH-TOCSY (22.5 ms mixing time), ^{13}C-TOCSY-HSQC (30 ms mixing time), ^{13}C-NOESY-HSQC (centered at the aliphatic region of 42.4 ppm, 50 ms mixing time), and ^{13}C-NOESY-HSQC (centered at the aromatic region of 121.7 ppm, 75 ms mixing time) spectra. In addition, a ^{1}H/^{13}C-HSQC spectrum was acquired on a sample containing 15% ^{13}C isotopic enrichment to enable stereospecific assignments for the methyl groups of leucine and valine (*24*), which were confirmed by analysis of a ct-HSQC spectrum (constant time delay of 0.0295 s) (*32*). An unlabeled sample was used to acquire homonuclear DQF-COSY (*33*), z-TOCSY (28 ms mixing time) (*27*), and NOESY spectra (50 ms mixing time) (*34*, *35*).

^{15}N Backbone Relaxation Measurements. The ^{15}N longitudinal and transverse relaxation rate constants, R_1 and R_2, respectively, were determined by collecting a time series of ^{15}N-HSQC spectra with an appropriate Rance-Kay type of sensitivity enhancement (*26*). R_1 and R_2 data sets were obtained using the relaxation delays of 0.01, 0.05, 0.11, 0.21, 0.43, 0.81, and 1.5 s for R_2 experiments and 0.01, 0.05, 0.11, 0.17, 0.23, and 0.35 s for R_1 experiments with duplicate measurements at all the time points. ^{15}N hard pulses were applied at a field strength of 10.2 kHz, while the decoupling was achieved by the multipulse sequence GARP1 (*36*) at 1.5 kHz. {^{1}H}−^{15}N steady-state NOE data sets were obtained by acquiring spectra with and without ^{1}H saturation prior to the beginning of the experiment. ^{1}H saturation was achieved by a series of 120° pulses (at a field strength of 7.5 kHz) applied 5 ms apart for a total of 3 s (*37*). Signals were averaged over 64 transients, with the delay between the transients for the R_1 (R_2) and NOE experiments being 3 and 2 s, respectively. Acquisition times along the t_2 (^{1}H) and t_1 (^{15}N) dimensions were 71.1 and 18.03 ms, respectively, while the spectral widths in the corresponding dimensions were 7200.7 and 1775.0 Hz, respectively. In all the experiments described above, the carrier for the proton frequency was kept on the water resonance.

The relaxation data were processed using NMRPipe (*38*). R_1, R_2, and heteronuclear NOE time domain data along t_1 were forward linear predicted once before application of a combination of cosine bell and a weak Lorentzian−Gaussian function, and only a cosine apodization was applied along the t_2 dimension. The data were zero filled once before Fourier transformation. The software package NMRView (*39*) was used for peak picking and calculation of peak intensities. The uncertainties in the peak heights were estimated from duplicated experiments, while R_1 and R_2 were calculated using FORTRAN codes developed in-house. Relaxation rate constants and related uncertainties were

determined by fitting the experimental points to a monoexponential function. Heteronuclear steady-state NOEs were determined as the ratio of the peak intensities with and without proton saturation.

For a heteronuclear two-unlike spin system, the relaxation rate constants (R_1 and R_2) and the steady-state heteronuclear NOE for the $^1H-^{15}N$ spin pair can be given by the power spectral density functions of the rotational motions at five frequencies $\omega = 0$, ω_N, $\omega_H - \omega_N$, ω_H, and $\omega_H + \omega_N$. In the reduced spectral density mapping approach, if it is assumed that $dJ(\omega)/d\omega^2$ is relatively constant between the linear combinations $\omega_H + \omega_N$ and $\omega_H - \omega_N$, the rate constants and NOE can be expressed as a linear combination of only three spectral density functions, $J(0)$, $J(\omega_N)$, and $J(0.87\omega_H)$. Following this procedure, the spectral density functions at these three frequencies in terms of the relaxation parameters can be written as (*40*, *41*)

$$J(0) = (6R_2 - 3R_1 - 2.72\sigma)/(3d^2 + 4c^2) \quad (1)$$

$$J(\omega_N) = (4R_1 - 5\sigma)/(3d^3 + 4c^2) \quad (2)$$

$$J(0.87\omega_H) = 4\sigma/5d^2 \quad (3)$$

where σ [$=(\mathrm{NOE} - 1)R_1\gamma_N/\gamma_H$] is the cross-relaxation rate of the spin pair and γ_H and γ_N are the gyromagnetic ratios of the ^1H and ^{15}N nuclei, respectively. $d = (\mu_o h\gamma_H\gamma_N/8\pi^2)\langle r_{NH}^{-3}\rangle$ and $c = \omega_N\Delta\sigma/\sqrt{3}$, where μ_o is the permeability of free space, h is Planck's constant, γ_H and γ_N are the gyromagnetic ratios of the ^1H and ^{15}N nuclei, respectively, and ω_N is the Larmor frequency of the ^{15}N spins at $B_o =$ 14.1 T (600 MHz). r_{NH} is the internuclear distance (1.02 Å), and $\Delta\sigma$ is chemical shift anisotropy of the ^{15}N spins (assumed to be -170.0 ppm for the amide nitrogen and -175.0 ppm for the indole nitrogen). For amide protons with limited intramolecular motions (determined by the ratio of R_1 to R_2), a local overall rotational correlation time, τ_m, is obtained from the spectral density functions:

$$\tau_m = \omega_N^{-1}[J(0) - J(\omega_N)/J(\omega_N)]^{1/2} \quad (4)$$

From the τ_m values, the amplitude of the intramolecular motion of the N−H bond vector in a molecular reference frame is defined as

$$S^2 = 5[J(0) - J(\omega_N)](1 + \omega_N^2\tau_M^2)/(2\omega_N^2\tau_M) \quad (5)$$

Equation 5 provides a good approximation of the square of the order parameter (S), in cases such as this where a model free approach to relaxation data analysis is not suitable.

Distance and Dihedral Angle Constraints. Interproton distance constraints were determined from cross-peak volume measurement obtained from the ^{15}N-NOESY-HSQC, ^{13}C-NOESY-HSQC, and homonuclear NOESY experiments (in D_2O, 50 ms mixing times) using the program FELIX (Accelrys). Standard calibration was performed using backbone, side chain, and methyl classes of protons. A set of upper bounds of 2.9, 3.5, and 5.0 Å or 2.7, 3.3, and 5.0 Å corresponding to strong, medium, and weak cross-peaks, respectively, were assigned for the ^{15}N-NOESY-HSQC and the ^{13}C-edited NOESY and ^1H-NOESY experiments, respectively. Lower bounds were set to the van der Waals radius value of 1.8 Å. Pseudoatom corrections were applied whenever stereospecific assignments were not available. Hydrogen bonding constraints (1.8 Å $\leq d_{HN-O} \leq$ 2.3 Å and 2.5 Å $\leq d_{N-O} \leq$ 3.3 Å) were used only if the amide proton exhibited significant signal intensity in the H−D exchange experiment 6 h after exchange and if the $^{\alpha}C$ chemical shift index and $^3J_{HN\alpha}$ values indicated well-defined secondary structure. ϕ angle restraints ($-65 \pm 25°$, $^3J_{HN\alpha} < 4.0$ Hz, or $-120 \pm 30°$, $^3J_{HN\alpha} > 8.0$) were assigned from the $^3J_{HN\alpha}$ coupling constant measurements obtained using either the 3D-HNHA or 2D-SCT-HMSQC-HA experiments. Additional ψ or χ constraints were not used.

Structure Calculations. Structures of L3[86] were calculated by simulated annealing using torsion angle dynamics in DYANA starting from 299 random conformers (*42*). The ratio of relative weights of upper limit, lower limit, van der Waals, and torsional constraints to target function calculations was set to 1:1:2:5. The stereospecific assignments were optimized using the HABAS algorithm in DYANA. Structures were calculated initially using only NOE-derived constraints. Then, hydrogen bond constraints were introduced, and finally, the torsional angle constraints were incorporated.

The qualities of the 20 best structures (based on the final target energy function in DYANA) were analyzed with AQUA and PROCHECK-NMR (*43*). Structures were visualized and figures generated using MOLMOL (*44*).

Structural Comparison with the XRCC1 BRCT Domains. The coordinates for the monomeric form of the XRCC1 BRCT domain (X1BRCTb, residues 538−629) in the crystal state (PDB entry 1CDZ) (*6*) was used for comparison with the average structure of L3[86] in solution by using the Kabsch and Sander algorithm and visualized using the program MOLMOL (*44*). Interhelical angles were measured using the method of Chothia incorporated in MOLMOL (*44*).

RESULTS AND DISCUSSION

Resonance Assignments. Sequence-specific assignments of nearly complete (>95% backbone and ~90% side chain) ^1H, ^{15}N, and ^{13}C resonances were obtained (available at the BioMagResBank database). In a few cases, aliphatic protons of residues with long side chains, such as Arg and Lys, could not be assigned unambiguously due to signal overlap in the ^1H dimension. In addition, some of the resonances belonging to the N-terminal residues (837−854) could not be assigned because the structure for this region is not well-defined. There are six prolines in the L3[86] sequence (P859, P860, P863, P899, P906, and P921). All proline peptide bonds are in the trans conformation as evidenced by strong $d_{\alpha i}d_{\delta(i+1)}$ NOEs (*45*).

Oligomeric State of L3[86]. Size-exclusion chromatography, dynamic light scattering, and NMR self-diffusion coefficient measurements, which were carried out under identical conditions as used in the structural study, indicate that L3[86] behaves as a homodimer in solution (*23*). In addition, mass spectrometry analysis showed that the experimentally determined mass is that as expected for a tightly associated dimer (*23*). A two-dimensional double-tuned isotope-filtered experiment acquired on a sample composed of an equal mixture of unlabeled and ^{13}C-labeled L3[86]

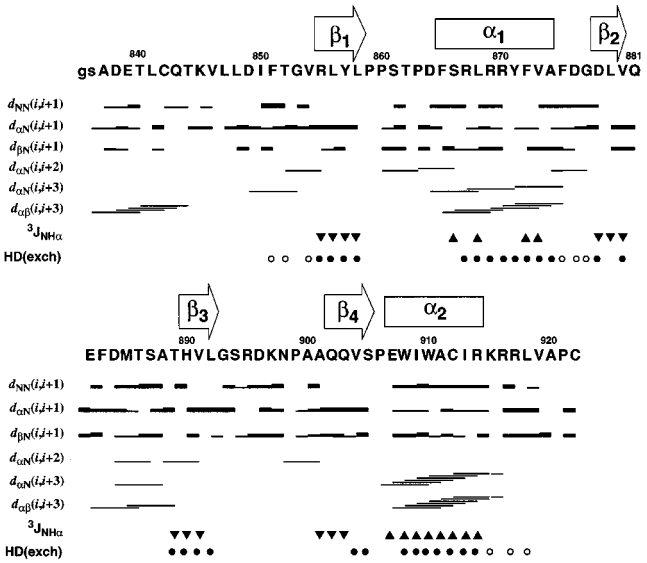

FIGURE 1: Summary of backbone NOE connectivities in the L3-[86] protein designated by thick, medium, and thin bands, which correspond to strong, medium, and weak cross-peaks, respectively, observed in the NOESY data. The deduced secondary structural elements are displayed over the sequence. The three-bond *J* couplings between the amide and H^{α} protons ($^3J_{NH\alpha}$) in the secondary structure regions are designated by the triangles. Residues that display slow amide exchange are designated by circles. Twenty-seven of these are located in regions having secondary structure (●), while nine are not within secondary structure regions (○).

explicitly identified residues V873 and A874 (located in α1) as being involved in dimer interactions. However, it was not possible to obtain additional unambiguous NOE restraints involving other residues that would aid in defining the dimer interface further. The reason for this result is most likely the low concentration (0.2 mM) of the ^{13}C-labeled protein, which was not expressed in yields as high as that of the ^{15}N or unlabeled protein. Furthermore, the concentration of the unlabeled−^{13}C-labeled complex would only comprise 50% of the sample, thereby reducing the concentration by half. Thus, only very strong intermolecular cross-peaks, such as those involving the V873 and A874 residues, could be observed. Consequently, only the structure of the monomer was determined. Nonetheless, the slow amide exchange rates of several residues indicate that they are protected from solvent, though they are not involved in secondary structural hydrogen bonding interactions [Figure 1(○)] and are located on the surface of the protein. One possible explanation for this behavior is that these residues are involved in intermolecular self-association interactions. In particular, the residues following A874 (F875, D876, and G877, which comprise the short loop between α1 and *β*2), residues F851, T852, and V854 (located in the N-terminus), and residues K915, R917, and L918 (located in the C-terminus) have slow amide exchange rates and no defined secondary structure. The regions that encompass parts of the N-terminus, α1, the α1−*β*2 loop, and the C-terminus identified by the isotope-filtered and H−D exchange experiments as the probable sites for dimerization in L3[86] happen to coincide with regions identified as the dimer interface in the crystal structure of X1BRCTb. Moreover, $R867^A$ and $D878^B$ and $D849^A$ and $R870^B$ (where A and B distinguish the two different monomeric units) can participate in salt bridges, like what has been observed in X1BRCTb for the homologous residues

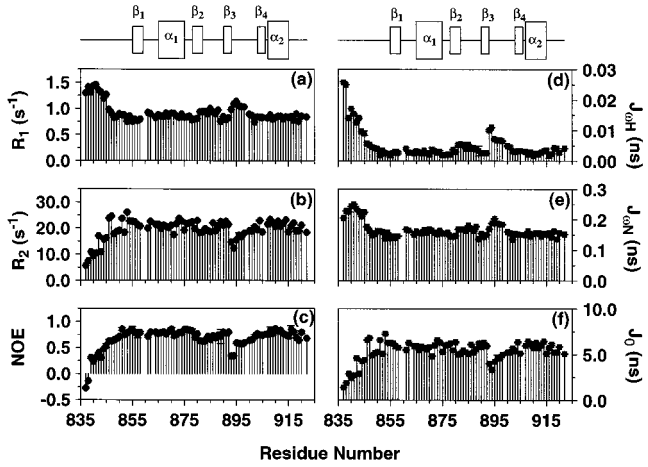

FIGURE 2: (Left) ^{15}N backbone amide R_1 (a) and R_2 (b) relaxation rates and $^{15}N-\{^1H\}$ NOE values plotted vs residue number in L3-[86]. The secondary structure elements are given at the top. (Right) The spectral density function, $J(\omega)$, with values at three frequencies: $0.87\omega_H$ (d), ω_N (e), and 0 (f).

(*6*). V873 and A874 coincide in the X1BRCTb structure with homologous valine and alanine residues that flank a threonine residue, which acts as central pivot point for the asymmetric dimer interface.

To shed more light on the oligomeric state of L3[86], measurements of the ^{15}N longitudinal (R_1) and transverse (R_2) relaxation rates (Table S1, Supporting Information) were used to determine the overall rotational correlation time, τ_c. An experimental τ_c value of 6.82 ± 1.003 ns was determined from trimmed (average values within one standard deviation) R_1/R_2 values. Empirical and theoretical estimates of τ_c based on correlations between τ_c and solvent accessible surface area (SASA) for a set of structures of proteins having similar molecular masses (∼10 kDa) (*46*) were 4.35 ± 0.05 and 3.55 ± 0.11 ns, respectively. The calculated τ_c value, on the other hand, based on the structure determined here and using the beads model theory of Garcia de la Torre and Bloomfield is 5.39 ns. The experimental τ_c value of 6.82 ± 1.003 ns that was obtained, which is greater than the estimated or calculated value, is consistent with L3[86] forming a dimer in solution.

^{15}N Backbone Relaxation Data. Residue-specific ^{15}N R_1 and R_2 relaxation rates and $^{15}N-\{^1H\}$ NOE values were measured for 82 residues (excluding the six prolines and including the two non-native N-terminal glycine and serine residues) observed in the ^{15}N-HSQC spectrum. The experimental values of R_1, R_2, and NOE are plotted versus residue number in Figure 2, and the values are listed in Table S1 of the Supporting Information. The average values of R_1 and R_2 for all 82 residues are 0.93 ± 0.8 and 19.5 ± 1.9 s^{-1}, respectively, and 0.87 ± 0.04 and 20.5 ± 1.2 s^{-1}, respectively, when the highly flexible N-terminal residues (835−845) were excluded. The variation pattern in the relaxation parameters closely follows the variability in the conformational space of L3[86] as determined by the NOE restraints. For example, the N-terminus of L3[86] has the fewest NOE constraints per residue (Figure 3), in agreement with the low $\{^1H\}-^{15}N$ heteronuclear NOE values (Figure 2c). The remaining residues do not exhibit large deviations from the average R_1, R_2, and heteronuclear NOE values, with the exception of the residues located in the long loop connecting

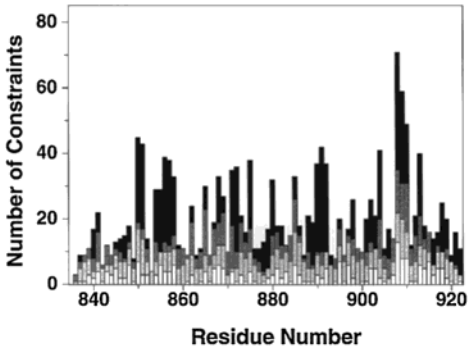

FIGURE 3: Distribution and number of strong (black), medium (gray), and weak (white) distance constraints for each residue along the sequence in L3[86].

β3 and β4. Smaller $\{^1H\}-^{15}N$ heteronuclear NOE values in this region correspond to smaller R_2 and larger R_1 values (Figure 2, and Table S1 of the Supporting Information). In particular, residues G893 and S894, which immediately follow β3, exhibit $\{^1H\}-^{15}N$ heteronuclear NOE values of <0.5.

To determine the time scales at which specific dynamic motions were occurring, the R_1, R_2, and NOE values were further analyzed using reduced spectral density mapping. Plots of the spectral density function, $J(\omega)$, values at three frequencies (0, ω_N, and $0.87\omega_H$; Figure 2d−f) suggest that high-frequency motions (ω_N and ω_H) in the nanosecond time scale range do not vary much from residue to residue (Figure 2d,e). In contrast, slow motions (ω_0) on the millisecond to microsecond time scale range are more variable across the protein backbone (Figure 2f), and the differences are more pronounced for both the N-terminal segment and the loop connecting β3 to β4. In general, however, the variation patterns in $J(0)$, $J(\omega_N)$, and $J(0.87\omega_H)$ are similar to those observed in R_2, R_1, and $^{15}N-\{^1H\}$ NOE, respectively (Table S1, Supporting Information).

The lack of significant residue-specific differences in the intramolecular motions, as in the case of L3[86], allows the use of $J(\omega)$ values to estimate the square of the order parameter (S^2), which measures the amplitude of the internal motion and its time scale (τ_m) (Figure 4b,c, and Table S2 of the Supporting Information). The majority of residues have S^2 values close to 1, which indicates that they are highly ordered (Figure 4c). However, the R_1/R_2 values plotted in Figure 4a do show a moderate variation in the backbone dynamics and suggest that certain regions, such as α2, are less flexible than others, in agreement with the slow amide exchange rates (Figure 1). In addition, the α2 helix contains two tryptophan residues (W908 and W910) that exhibit dynamical differences. Whereas W908 is a highly conserved residue in the BRCT family and a mutation of the homologous tryptophan (W1837) to an arginine in the BRAC1 protein is known to predispose patients to cancer, W910 is not conserved (*6*). Relaxation parameters of the indole NH vector of both tryptophans are close to each other (Table 1), suggesting that they both undergo very similar motions on the nanosecond time scale. The R_2 values are identical and close to that observed for several other backbone amide vectors (Table S1, Supporting Information), showing that the differences in motions occurring on the microsecond time scale are also negligible. In contrast, significant differences in the amide proton exchange behavior are observed. While

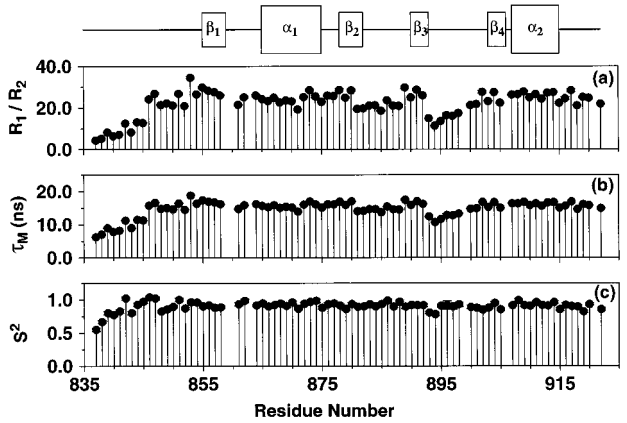

FIGURE 4: Model dynamic parameters: (a) R_1/R_2 values, (b) local rotational correlation time (τ_m), and (c) the square of the order parameter (S^2) plotted vs residue number in L3[86].

Table 1: Summary of Tryptophan Side Chain Dynamics

parameter	W908	W910
R_1 (s^{-1})	0.70 ± 0.01	0.69 ± 0.02
R_2 (s^{-1})	17.94 ± 0.09	16.57 ± 0.08
NOE	0.79 ± 0.04	0.79 ± 0.05
$J(0)$ (ns)	4.9 ± 0.02	4.51 ± 0.02
$J(\omega_N)$ (ns)	0.13 ± 0.00	0.13 ± 0.00
$J(\omega_H)$ (ns)	0.002 ± 0.000	0.002 ± 0.000
S^2 (order parameter)	0.76 ± 0.02	0.73 ± 0.02
τ_m (ns)	16.06 ± 0.06	15.45 ± 0.05
no. of long-range NOEs	12	6
k_{ex}^{HD} (min^{-1})	$(4.45 \pm 0.03) \times 10^{-3}$	$>3.3 \times 10^{-2}$

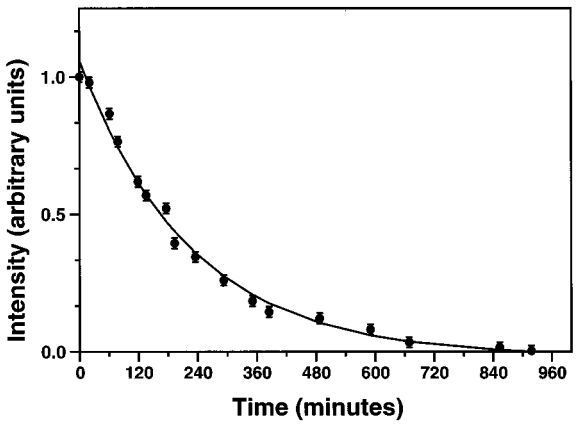

FIGURE 5: Plot of the relative intensity of the W908 indole proton in an HSQC spectrum as a function of time after solvent exchange from H_2O to D_2O (0 point is ~150 min after exchange). The solid line is an exponential fit to the experimental data, assuming a first-order exchange process.

the indole proton resonance of W910 is unobservable in the first HSQC spectrum obtained approximately 150 min after the H−D exchange, the W908 indole NH could be monitored for at least 3 days. If a first-order exchange process is assumed, an exponential fit to the experimental data produces an exchange rate of $(4.45 \pm 0.02) \times 10^{-3}$ min^{-1} for the W908 indole NH (Figure 5). Numerous medium- and long-range NOE cross-peaks were observed from the indole proton of W908 to several surrounding conserved residues (L918, V919, A920, P921, and C922), as well as to a highly conserved cysteine (C912). In fact, W908 displays the greatest number of NOEs per residue (Figure 3). The H−D and NOE results are consistent with W910 being located on

the surface and accessible to solvent exchange, while W908 is buried in the hydrophobic core of the structure of the protein. This suggests that one potential structural consequence of mutations involving the conserved W908 would be to hinder the formation of a properly folded BRCT domain.

Structure Determination. Elements of regular secondary structure were identified on the basis of three criteria: (1) NOE patterns, (2) the three-bond *J* coupling between the amide and H^{α} protons ($^3J_{NH\alpha}$), and (3) the amide proton solvent-exchange rates (Figure 1). Chemical shift indices (CSI) for H^{α}, C^{α}, CO, and C^{β} resonances were also determined and used to confirm the secondary structure assignments (Figure S1, Supporting Information). The results indicate the presence of two α-helices [α1 (residues F865−A874) and α2 (residues E907−R914)] and four *β*-strands [*β*1 (residues R855−L858), *β*2 (residues D878−V880), *β*3 (residues H890−L892), and *β*4 (residues Q902−S905)] (Figure 1). Helices α1 and α2 are defined by NOEs between H^{α}_i and H^{N}_{i+3} and between H^{α}_i and H^{β}_{i+3} (*45*) and by their CSI values. The *β*-strands were determined primarily from the CSI values (*47*) and by the absence of strong NOEs between H^{N}_i and H^{N}_{i+1}, which suggests extended structures (*45*). The parallel *β*2*β*1*β*3*β*4 strand alignment for the *β*-sheet was defined by the long-range NOEs between the amide proton of a residue in one strand and the H^{α} proton of a residue in its neighboring strand.

A total of 36 slowly exchanging amide protons were identified from the ^{15}N-HSQC spectrum acquired approximately 6 h after solvent exchange with D_2O (Figure 1). Twenty-seven of these residues are located in regions having defined secondary structure and provide the 54 hydrogen bonding restraints used in the structure calculations [Figure 1 (●)]. The secondary structure of N-terminal residues A837−V854 is not well-defined and appears to be disordered, as indicated by the CSI values (Figure S1, Supporting Information) and the smaller number of NOEs observed for this region (Figure 3). However, some unusual characteristics (backbone relaxation parameters and slow amide exchange) are evident for several residues in this segment. Residues A837−T844 exhibit partial helical character as evidenced by the presence of H^{α}_i to H^{β}_{i+3} medium-range NOEs. Still, they show neither the expected H^{α}_i to H^{N}_{i+3} connectivities nor the CSI for an α-helix (Figure S1, Supporting Information). Although exchange cross-peaks were not observed, these results may be partially explained by a fast conformational exchange between a helix and coil. This would result in the average structure of a poorly defined helix being observed on the NMR time scale.

The ^{1}H-NOESY, ^{13}C-edited NOESY, and ^{15}N-edited NOESY spectra yielded a total of 979 unique NOE-derived upper distance limits (Table 2 and Figure 3). An additional 54 hydrogen bond distance restraints and 25 dihedral angle restraints were also acquired for a total of 12.5 restraints per residue (Table 2). These restraints, along with the chemical shift assignments, can be found as PDB entry 1IMO.

A final family of 20 structures out of 299 calculated in DYANA had the lowest number of restraint violations (Figure 6). A distribution of the calculated structures as a function of the final target energy values shows that the 20 final structures also exhibited the lowest energy values. This family of 20 structures has an average rmsd of 0.58 ± 0.15 Å for backbone atoms and 1.18 ± 0.18 Å for all residues from A837 to C922 (Table 2). The average rmsd from the mean structure for the backbone heavy atoms (residues 855−905, omitting the residues in the disordered N-terminus, the *β*3−*β*4 loop, and the C-terminus) is 0.27 ± 0.09 Å for backbone atoms and 1.10 ± 0.21 Å for all the heavy atoms. None of the distance or dihedral angle violations were greater than 0.3 Å or 5.0°, respectively, in the structure family. Ramachandran plot analysis in PROCHECK-NMR (*43*) shows that of the residues located in the secondary structure region of the protein, 72.2% of the *φ* and *ψ* angles lie within the most favored region, 27.8% in the additionally favored region, and none in the generously allowed or disallowed regions (Figure S2, Supporting Information). When all the residues are considered, 49.1% lie within the most favored region and 41.9% in the additionally allowed regions of the Ramachandran plot. Those residues with *φ* and *ψ* angles falling within the generously allowed or disallowed regions are generally located in the disordered parts of the structures, with no consensus among the family members for any particular residue to be within the disallowed region. As expected, however, surface-exposed side chains, especially those from arginine and lysine, tend to show the greatest disorder and subsequently are the residues most frequently found in the disallowed region.

Table 2: Statistics for the Family of 20 Structures and the Average Structure

total no. of interproton restraints	979
intraresidue	252
sequential ($\|j - i\| < 2$)	228
medium-range ($\|j - i\| < 5$)	144
long-range ($\|j - i\| > 4$)	355
no. of hydrogen bonds	54
no. of dihedral angles	25
stereospecific assignments of Leu and Val	14/16
total no. of restraints	1072
total no. of restraints per residue	12.5

	secondary structure	all
backbone rmsd (Å)	0.27 ± 0.09	0.58 ± 0.09
all heavy atom rmsd (Å)	1.10 ± 0.21	1.18 ± 0.18
average target function (Å^2)		17.3 ± 1.4
largest upper restraint violation (Å)		0.28 ± 0.06
largest lower restraint violation (Å)		0.08 ± 0.01
largest van der Waals violation (Å)		0.15 ± 0.04
Ramachandran plot statistics (Figure S2, Supporting Information)		
residues in most favored regions (%)	77.2	
residues in additional allowed regions (%)	27.8	
residues in generously allowed regions (%)	0.0	
residues in disallowed regions (%)	0.0	

Description of the Structure. L3[86] forms a compact α/*β*-structure consisting of a core four-stranded parallel *β*-sheet with a *β*2*β*1*β*3*β*4 strand order and two α-helices (α_1 and α_2) packed against one side of the sheet. Two large loops (*β*2−*β*3 and *β*3−*β*4) are located on the opposite face of the *β*-sheet (Figure 6). The first several residues in the N-terminal domain adopt a poorly defined helical turn that forms hydrophobic packing interactions with α2. The overall topology is *β*1α1*β*2*β*3*β*4α2. To visualize the backbone dynamics of L3[86], the order parameter (Figure 4) deter-

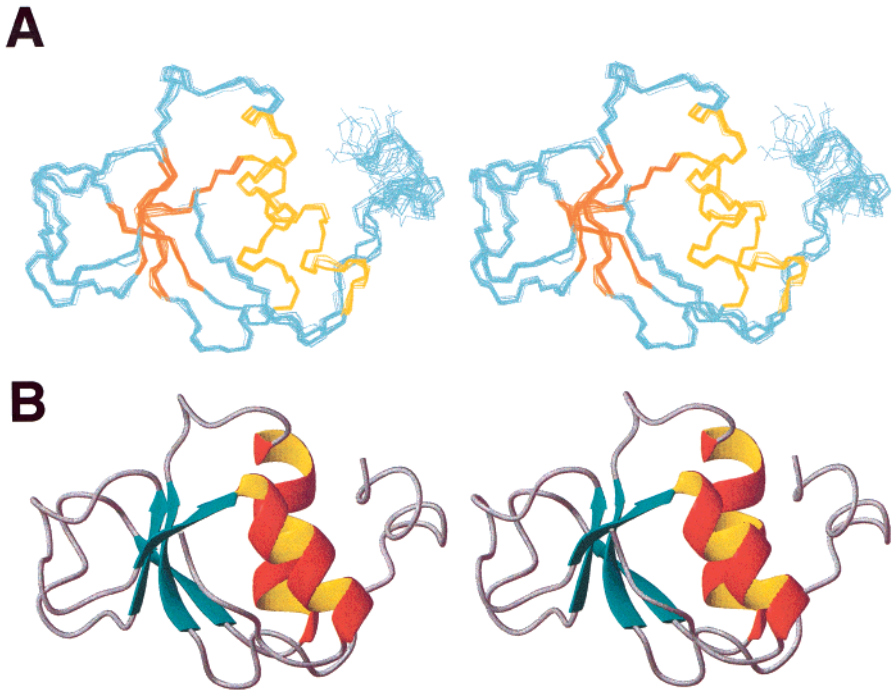

FIGURE 6: Stereodiagrams of (A) the superimposed ensemble of 20 structures (β-strands in red, α-helices in gold, and loops in cyan) and (B) the average structure (β-strands in blue and α-helices in red and gold).

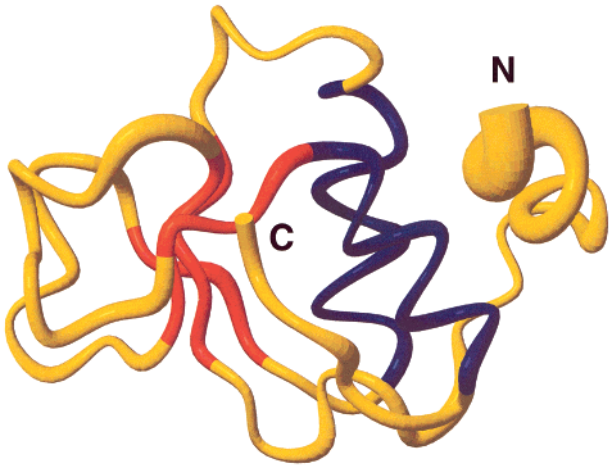

FIGURE 7: Superposition of the order parameter determined from the relaxation experiments and reduced spectral density mapping onto the L3[86] backbone.

mined from the relaxation experiments and reduced spectral density mapping was superimposed on the protein backbone (Figure 7). The variation in the backbone radius is scaled in proportion to the order parameter. Nanosecond time scale motions are fairly constant, with the largest movements observed for the loop regions and the N-terminal segment.

Comparison with Other Structurally Homologous Domains. A search of the SCOP (Structural Classification of Proteins) database (*48*) yielded several proteins with folds that are homologous to the L3[86] fold, though they all exhibit very low levels of sequence homology. In these cases, the minimal structural motif that defined similarity to the structure of L3[86] is the core four-stranded parallel β-sheet with a $\beta2\beta1\beta3\beta4$ order with a two-helix bundle packed against one face of the β-sheet. The minimal structural motif happens to coincide with the most conserved regions of the BRCT family (*2*, *5*). The major difference between the structures of L3[86] and these structural homologues was the presence of one or more additional helices located on the opposite face of the β-sheet. These structural elements were also found to be the least conserved in the BRCT family (*2*, *5*). In all cases but one, this fold was found to stabilize orderly self-associations to higher oligomeric states by specific protein−protein interactions. For example, 60 β-subunits of lumazine synthase (PDB entry 1rvv) interact predominantly though their α-helices to form an icosahedral shell (*49*). Similarly, the caspase-like N-terminal domain of the gingipain R protein [PDB entry 1cvr (*50*)] and the catalytic domain of malonyl-CoA ACP transacylase [PDB entry 1mla (*51*)] interact through their α-helices to form dimers.

Another example of a protein−protein interaction module with a similar fold is the structure of X1BRCTb (*6*), which is the binding partner of L3[86] (*52*) (Figure 8). Three major differences in sequence between L3[86] and X1BRCTb are that L3[86] is nine residues longer at the N-terminus, eight residues shorter at the C-terminus, and missing the ten residues comprising the X1BRCTb α2 helix, the sequence of which is the least conserved among the BRCT family (*23*). The sequences and structural positions of the L3[86] and X1BRCTb α1 helices, as well as the packing alignment between α1 and α2 (X1BRCTb α3), are also conserved. The interhelical angle between these helices is 36.2° in L3[86] and 43.2° in X1BRCTb. Like the interactions observed between α1 and α3 in the X1BRCTb structure, the L3[86] α1 L868, Y871, and V873 residues form hydrophobic packing interactions with the α2 I909 and W910 residues. The difference in the overall solvent accessible surface area between the structures of X1BRCTb (5920 Å^2) and L3[86] (4853.1 Å^2) (calculated from the average structure) reflects two differences that distinguish the structures, namely, the number of helices (three α-helices vs two) and the difference in the length of α1 (Figure 8).

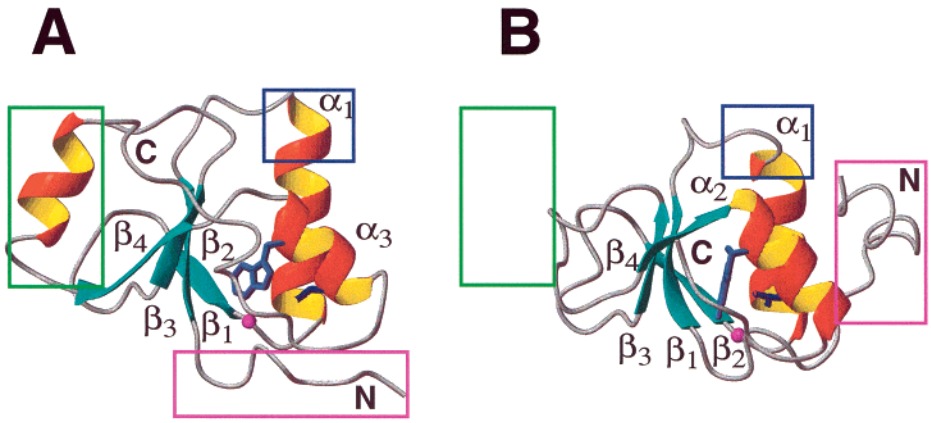

FIGURE 8: Comparison of the structures of (A) X1BRCTb (*6*) and (B) L3[86] (*β*-strands in cyan and α-helices in red and gold). Views are positioned so that the two conserved helices (α1 and α2 in L3[86] and α1 and α3 in X1BRCTb) are aligned. The highly conserved residues W908 and C910 in L3[86] and W611 and C615 in X1BRCTb are shown in blue. The three major differences between the structures are highlighted by the matching colored boxes. The nine-residue longer N-terminal region in L3[86] is able to fold back and make contacts with α2 (magenta). The α1 helix is four residues shorter in the L3[86] structure (blue). The entire X1BRCT α2 sequence and corresponding helix is missing in the L3[86] structure (green).

One other class of proteins that have folds similar to that of L3[86], but do not participate in protein−protein interactions, are the repair proteins uracil-DNA glycosylase [PDB entry 1akz (*53*)] and G:T/U mismatch specific DNA glycosylases. Interestingly, unlike the helix−helix contacts that were found to predominate in forming the protein−protein interactions, a hydrophobic pocket composed of the *β*-sheet and flanking helices binds the looped out uracil base in the crystal structure of the uracil-DNA glycosylase−DNA complex (PDB entry 1emh). In addition, the glycosylases adopt monomeric structures.

We find that the *β*2*β*1*β*3*β*4 parallel sheet with a two-helix bundle unit is a highly conserved structural scaffold. The examples given here of proteins that exhibit similar structural folds but have a wide range of functions imply that sequence differences are important in specifying the type of interactions that these folds enable. It will be interesting to determine if other BRCT domains adopt similar core structures and to relate how both structure and sequence differences are used to provide partner specificity.

Potential Protein−Protein Interaction Surface. Previously, we prepared two different heterocomplexes of the XRCC1/L3 BRCT domains for biophysical characterization to provide insight into the interaction between these two BRCT binding partners (*23*). Unfortunately, the NMR data for the complexes exhibited narrow lines mixed with very broad lines, which hindered detailed structural studies. Size-exclusion chromatography studies show that both complexes elute as dimers at low concentrations and as tetramers (homodimers of L3 BRCT and X1BRCTb) at the high concentrations (9 mg/mL) needed for NMR studies (*23*). Higher-order aggregates were also observed at very high concentrations (23 mg/mL). The formation of a tetrameric L3[86]−X1BRCTb complex implies that the homodimer and the heterodimer interfaces cannot be the same. However, this result directly contradicts a recent combined modeling and mutation study of a X1BRCTb−L3 BRCT complex which predicts that the heterodimer and homodimer interfaces are the same (*54*). In contrast, Taylor et al. (*52*) have identified a different region, comprised of the region centered around the *β*2−*β*3 loop, residues 573−592 in X1BRCTb, as the minimal region that binds to L3α. An obvious next step in our investigations will be to better define these regions and their involvement in complex formation.

ACKNOWLEDGMENT

We are grateful to Dr. Alan Tomkinson for the GSTag-L3α expression vector and to Dr. Rod Balhorn for critical reading and comments on the manuscript.

SUPPORTING INFORMATION AVAILABLE

Table S1 listing the R_1 and R_2 relaxation rates and the heteronuclear NOE values, Table S2 listing the $J(\omega)$ values and order parameter (S^2) values, Figure S1 showing the chemical shift index for secondary structure, and Figure S2 showing the Ramachandran plot. This material is available free of charge via the Internet at http://pubs.acs.org.

REFERENCES

1. Koonin, E. V., Altschul, S. F., and Bork, P. (1996) *Nat. Genet. 13*, 266−268.
2. Bork, P., Hofmann, K., Bucher, P., Neuwald, A. F., Altschul, S. F., and Koonin, E. V. (1997) *FASEB J. 11*, 68−76.
3. Gayther, S. A., Mangion, J., Russell, P., Seal, S., Barfoot, R., Ponder, B. A., Stratton, M. R., and Easton, D. (1997) *Nat. Genet. 15*, 103−105.
4. Yamane, K., Kawabata, M., and Tsuruo, T. (1997) *Eur. J. Biochem. 250*, 794−799.
5. Callebaut, I., and Mornon, J. P. (1997) *FEBS Lett. 400*, 25−30.
6. Zhang, X. D., Morera, S., Bates, P. A., Whitehead, P. C., Coffer, A. I., Hainbucher, K., Nash, R. A., Sternberg, M. J. E., Lindahl, T., and Freemont, P. S. (1998) *EMBO J. 17*, 6404−6411.
7. Kubota, Y., Nash, R. A., Klungland, A., Schar, P., Barnes, D. E., and Lindahl, T. (1996) *EMBO J. 15*, 6662−6670.
8. Caldecott, K. W., Aoufouchi, S., Johnson, P., and Shall, S. (1996) *Nucleic Acids Res. 24*, 4387−4394.
9. Marintchev, A., Robertson, A., Dimitriadis, E. K., Prasad, R., Wilson, S. H., and Mullen, G. P. (2000) *Nucleic Acids Res. 28*, 2049−2059.
10. Masson, M., Niedergang, C., Schreiber, V., Muller, S., Menissier-deMurcia, J., and deMurcia, G. (1998) *Mol. Cell. Biol. 18*, 3563−3571.
11. Marintchev, A., Mullen, M. A., Maciejewski, M. W., Pan, B., Gryk, M. R., and Mullen, G. P. (1999) *Nat. Struct. Biol. 6*, 884−893.

12. Cappelli, E., Taylor, R., Cevasco, M., Abbondandolo, A., Caldecott, K., and Frosina, G. (1997) *J. Biol. Chem. 272*, 23970−23975.
13. Wilson, S. H., and Singhal, R. K. (1998) in *DNA Damage and Repair*: *DNA Repair in Higher Eukaryotes* (Nickoloff, J. A., and Hoekstra, M. F., Eds.) pp 161−180, Humana Press, Totowa, NJ.
14. Tomkinson, A. E., Roberts, E., Daly, G., Totty, N. F., and Lindahl, T. (1991) *J. Biol. Chem. 266*, 21728−21735.
15. Chen, J., Tomkinson, A. E., Ramos, W., Mackey, Z. B., Danehower, S., Walter, C. A., Schultz, R. A., Besterman, J. M., and Husain, I. (1995) *Mol. Cell. Biol. 15*, 5412−5422.
16. Colinas, R. J., Goebel, S. J., Davis, S. W., Johnson, G. P., Norton, E. K., and Paoletti, E. (1990) *Virology 179*, 267−275.
17. Kerr, S. M., Johnston, L. H., Odell, M., Duncan, S. A., Law, K. M., and Smith, G. L. (1991) *EMBO J. 10*, 4343−4350.
18. Wei, Y. F., Robins, P., Carter, K., Caldecott, K., Pappin, D. J. C., Yu, G. L., Wang, R. P., Shell, B. K., Nash, R. A., Schar, P., Barnes, D. E., Haseltine, W. A., and Lindahl, T. (1995) *Mol. Cell. Biol. 15*, 3206−3216.
19. Mackey, Z. B., Ramos, W., Levin, D. S., Walter, C. A., McCarrey, J. R., and Tomkinson, A. E. (1997) *Mol. Cell. Biol. 17*, 989−998.
20. Chew, S. L., Baginsky, L., and Eperon, I. C. (2000) *Nucleic Acids Res. 28*, 402−410.
21. Tomkinson, A. E., and Levin, D. S. (1997) *BioEssays 19*, 893−901.
22. Lakshmipathy, U., and Campbell, C. (2000) *Nucleic Acids Res. 28*, 3880−3886.
23. Thornton, K. H., Krishnan, V. V., West, M. G., Popham, J., Ramirez, M., Thelen, M. P., and Cosman, M. (2001) *Protein Expression Purif. 21*, 401−411.
24. Neri, D., Szyperski, T., Otting, G., Senn, H., and Wüthrich, K. (1989) *Biochemistry 28*, 7510−7516.
25. Pace, C. N., Vajdos, F., Fee, L., Grimsley, G., and Gray, T. (1995) *Protein Sci. 4*, 2411−2423.
26. Kay, L. E., Keifer, P., and Saarinen, T. (1992) *J. Am. Chem. Soc. 114*, 10663−10665.
27. Cavanagh, J., and Rance, M. (1992) *J. Magn. Reson. 96*, 670−678.
28. Talluri, S., and Wagner, G. (1996) *J. Magn. Reson., Ser. B 112*, 200−205.
29. Grzesiek, S., and Bax, A. (1992) *J. Magn. Reson. 96*, 432−440.
30. Altieri, A. S., Hinton, D. P., and Byrd, R. A. (1995) *J. Am. Chem. Soc. 117*, 7566−7567.
31. Cavanagh, J. (1996) *Protein NMR spectroscopy*: *Principles and Practice*, Academic Press, San Diego.
32. Diercks, T., Schwaiger, M., and Kessler, H. (1998) *J. Magn. Reson. 130*, 335−340.
33. Rance, M., Sørensen, O. W., Bodenhausen, G., Wagner, G., Ernst, R. R., and Wüthrich, K. (1983) *Biochem. Biophys. Res. Commun. 117*, 479−485.
34. Jeener, J., Meier, B. H., Bachmann, P., and Ernst, R. R. (1979) *J. Chem. Phys. 71*, 4546−4553.
35. Kumar, A., Ernst, R. R., and Wüthrich, K. (1980) *Biochem. Biophys. Res. Commun. 95*, 1−6.
36. Shaka, A. J., Barker, P. B., and Freeman, R. (1985) *J. Magn. Reson. 64*, 547−552.
37. Markley, J. L., Horsley, W. J., and Klein, M. P. (1971) *J. Chem. Phys. 55*, 3604−3605.
38. Delaglio, F., Grzesiek, S., Vuister, G. W., Zhu, G., Pfeifer, J., and Bax, A. (1995) *J. Biomol. NMR 6*, 277−293.
39. Johnson, B. A., and Blevins, R. A. (1994) *J. Biomol. NMR 4*, 603−614.
40. Ishima, R., and Nagayama, K. (1995) *Biochemistry 34*, 3162−3171.
41. Farrow, N. A., Zhang, O. W., Szabo, A., Torchia, D. A., and Kay, L. E. (1995) *J. Biomol. NMR 6*, 153−162.
42. Güntert, P., Mumenthaler, C., and Wüthrich, K. (1997) *J. Mol. Biol. 273*, 283−298.
43. Laskowski, R. A., Rullmannn, J. A., MacArthur, M. W., Kaptein, R., and Thornton, J. M. (1996) *J. Biomol. NMR 8*, 477−486.
44. Koradi, R., Billeter, M., and Wüthrich, K. (1996) *J. Mol. Graphics 14*, 51−55, 29−32.
45. Wüthrich, K. (1986) *NMR of Proteins and Nucleic Acids*, Wiley, New York.
46. Krishnan, V. V., and Cosman, M. (1998) *J. Biomol. NMR 12*, 177−182.
47. Wishart, D. S., Bigam, C. G., Yao, J., Abildgaard, F., Dyson, H. J., Oldfield, E., Markley, J. L., and Sykes, B. D. (1995) *J. Biomol. NMR 6*, 135−140.
48. Murzin, A. G., Brenner, S. E., Hubbard, T., and Chothia, C. (1995) *J. Mol. Biol. 247*, 536−540.
49. Ritsert, K., Huber, R., Turk, D., Ladenstein, R., Schmidt-Bäse, K., and Bacher, A. (1995) *J. Mol. Biol. 253*, 151−167.
50. Eichinger, A., Beisel, H. G., Jacob, U., Huber, R., Medrano, F. J., Banbula, A., Potempa, J., Travis, J., and Bode, W. (1999) *EMBO J. 18*, 5453−5462.
51. Serre, L., Verbree, E. C., Dauter, Z., Stuitje, A. R., and Derewenda, Z. S. (1995) *J. Biol. Chem. 270*, 12961−12964.
52. Taylor, R. M., Wickstead, B., Cronin, S., and Caldecott, K. W. (1998) *Curr. Biol. 8*, 877−880.
53. Mol, C. D., Arvai, A. S., Slupphaug, G., Kavli, B., Alseth, I., Krokan, H. E., and Tainer, J. A. (1995) *Cell 80*, 869−878.
54. Dulic, A., Bates, P. A., Zhang, X. D., Martin, S. R., Freemont, P. S., Lindahl, T., and Barnes, D. E. (2001) *Biochemistry 40*, 5906−5913.

BI010979G